

Identifying Dynamic Modes of Separated Flow Subject to ZNMF-based Control from Surface Pressure Measurements

Eric Deem*, Louis Cattafesta†

Mechanical Engineering, Florida State University, Tallahassee, FL, 32310

Hao Zhang‡, Clarence Rowley §

Mechanical and Aerospace Engineering, Princeton University, Princeton, NJ, 08544

Maziar Hemati¶

Aerospace Engineering and Mechanics, University of Minnesota, Minneapolis, MN, 55455

Francois Cadieux||, and Rajat Mittal **

Mechanical Engineering, Johns Hopkins University, Baltimore, MD, 21218

May 15, 2017

Fluid systems are most efficient for fully attached flows, and designers therefore seek to avoid flow separation. Active flow control can help achieve this goal, and closed-loop control offers improved performance at off-design conditions. However, this requires feedback of accurate state estimates to the controller in real time. This motivates a physics-based, state-estimation technique that economically extracts key dynamical features of the flow. This work aims to extract dynamical characteristics of a laminar separation bubble on a flat plate at a chord Reynolds number of 10^5 using a linear array of unsteady surface pressure measurements. First, Dynamic Mode Decomposition (DMD) is employed on high-dimensional time-resolved PIV velocity and corresponding estimated pressure fields to identify the dynamically relevant spatial structure and temporal characteristics of the separated flow. Then, results are presented of various open-loop control cases using pulse-modulation of a zero-net mass-flux actuator slot located just upstream of separation. Real-time estimates of the dynamical characteristics are provided by performing on-line DMD on measurements from a linear array of 13 unsteady surface pressure transducers. The results show that this method provides reliable estimates of the modal characteristics of the separated flow subject to forcing at a rate much faster than the characteristic time scales of the flow. Therefore, online DMD applied to the surface pressure measurements provides a time-varying linear estimate of the evolution of the controlled flow, thereby enabling closed-loop control.

I. Introduction

Aircraft, wind turbines, turbomachinery, and other fluid systems operate optimally with fully attached flow. The performance envelopes of these systems are therefore limited by the onset of flow separation. As such, efficient active control strategies for eliminating or delaying flow separation have been studied extensively and have garnered significant attention in various industries involving fluid systems. However, a universal approach to control this phenomena has been so far elusive. This work seeks towards providing a physics-based framework for closed-loop separation control that is applicable over a wide range of flow conditions and separated flow characteristics.

The available active flow control literature is rich with examples of various active flow control techniques for mitigating flow separation. The most common is an open-loop approach, in which the control parameters are determined beforehand, via physical insight or parametric studies. Since there is no state feedback in open-loop control, optimal control that is robust to disturbances and parameter variations cannot be achieved. Nonetheless, effective open-loop separation control strategies have been developed that exploit various flow characteristics in a favorable way. Considering the case of nominally two-dimensional separation, Seifert et al. compare the effect pulsed control has versus steady actuation and find that control authority is increased substantially when an unsteady component is introduced.¹ This observation introduces the unsteady actuation frequency and waveform as control parameters. As such, experimental and computational studies have been conducted in order to determine optimal forcing frequencies.²⁻⁶

As explained in Mittal et al.⁷ up to 3 characteristic frequencies exist for an uncontrolled separated flow. The first frequency is the wake shedding frequency f_{wake} . Second, small disturbances in the separated shear layer grow to large vortical structures via the Kelvin-Helmholtz instability with a shear layer frequency f_{sl} . Finally, if the separated shear

*PhD Candidate and AIAA Member

†Professor and AIAA Associate Fellow

‡PhD Candidate and AIAA Member

§Professor and AIAA Associate Fellow

¶Assistant Professor and AIAA Member

||Postdoctoral Fellow and AIAA Member. Current position: Research Scientist, NASA Advanced Supercomputing, Moffett Field, CA

**Professor and AIAA Associate Fellow

layer reattaches to the surface to form a closed separation bubble, the frequency corresponding to the meandering of the reattachment point is referred to as the separation bubble frequency f_{sep} . Additionally, Kotapati et al.⁸ show that these frequencies exhibit triadic lock-on interactions in some cases, indicating that nonlinearities exist that can be exploited for efficient separation control.

Irrespective of the form of actuation, several studies have shown that efficient control is achieved for forcing frequencies near the frequency of the shear layer instability.^{9–12} Recently, Griffin et al.¹³ provide results of varying the actuation frequency of a ZNMF jet in the vicinity of the characteristic frequencies of a canonical separated flow. The authors find that forcing near the shear layer frequency has the most dramatic impact on reducing separation. This result is corroborated by the work by Hemati et al.¹⁴ in which a noise-robust variant of Dynamic Mode Decomposition (DMD) is utilized to evaluate a set of candidate forcing frequencies. DMD is amenable to identifying dynamical characteristics of the separated flow field since the periodic phenomena are distributed throughout the flow and DMD identifies the frequencies of spatially coherent modes that are distinguished by temporal frequency.^{15,16} Of the candidate frequencies identified in this work, forcing at the frequency that corresponded to the shear layer mode exhibits the best performance in terms of reducing the height of the separation region.

In contrast to the aforementioned works, the computational study by Raju et al. suggests that forcing at the separation bubble frequency is preferred versus the shear layer frequency.⁶ However, significant differences exist between these two configurations, e.g., model geometry, relative actuation location, etc. As such, it is unlikely that a universal optimal forcing frequency can be determined, since the flow characteristics, model geometry, and control schemes can vary.

Linear stability analyses have been utilized to guide the control of separated flow and to aid in interpreting the effect of forcing. Recently, the work by Marxen et al.¹² provides results of linear stability analysis of a simulated canonical separated flow subject to forcing. Additionally, linear stability analysis of PIV measurements of a laminar separation bubble undergoing dielectric barrier discharge plasma forcing are provided in the work by Yarusevych and Kotsonis.¹¹ Both studies show that effective control occurs when the forcing frequency is sufficiently close to the frequency identified by the stability analysis to provide the highest amplification. This frequency corresponds to the preferred frequency of the shear layer roll up by the Kelvin-Helmholtz instability.¹² However, deformation of the mean flow by the actuation serves to alter the stability characteristics of the flow. Specifically, the frequencies identified by the stability analyses decrease commensurate with the reduction in the mean separation region.^{11,12} This suggests that further reduction in the separation region may be possible by accounting for the variation in the characteristic frequencies once forcing is applied. In fact, Marxen et al. show justification that the greatest separation reduction may occur when the forcing frequency is near the most amplified frequency identified by linear stability analysis of the controlled flow (as opposed to that of the uncontrolled flow)¹². Of course, this requires knowledge of the controlled flow state.

This provides motivation for closed-loop separation control. Since many factors contribute to the performance of the control approach, having the flow states monitored and fed back to the controller can provide robustness to changes in airfoil geometry, separation characteristics, stability qualities, and flow conditions. However, several questions must be answered in order to accomplish this goal. For instance, given technological and practical constraints, how should the dynamical states of the flow be measured and fed back into the controller? What is the global effect various forms of actuation have on the flow field? How receptive are the states to actuation? Finally, how does one properly pose the mathematical control objective for reducing flow separation?

To this end, advanced flow diagnostic tools and analyses are employed to identify modalities of the separated flow field subjected to actuation. Since full-field velocity data is too cumbersome to include in a practical separation control platform, dynamic mode decomposition (DMD) of unsteady surface pressure information is applied to identify the separated flow modes. This provides a discrete linear representation of the flow from an array of unsteady surface pressure data. Furthermore, since actuation serves to alter the mean and dynamic characteristics of the flow, system estimates must be updated to account for these variations. This is accomplished by employing a new, recursive algorithm called online DMD,¹⁷ in which linear system updates are provided with each new snapshot. This manuscript proceeds with a description of the experimental setup and numerical procedures, analysis of the baseline and actuated flow field characteristics from full field flow measurements, and the results of applying online DMD to estimate the separated flow dynamics subject to forcing.

II. Experimental Setup

An experimental approach is taken to facilitate the analysis of two-dimensional laminar flow separation subject to control by a ZNMF jet actuator. A canonical separated flow configuration is utilized to remove dependencies on curvature. Specifically, an adverse pressure gradient is imposed causing a laminar boundary layer to separate from a flat plate model in a wind tunnel facility.

This section provides details regarding the experimental design, data collection, and the methods used for processing and analyzing the results. The wind tunnel facility is described, followed by specific information regarding the experimental model and flow separation system. Then, the data collection methods including surface mounted pressure

sensors and particle image velocimetry (PIV) are described in detail. Finally, the manner in which the collected data are handled is outlined.

A. Wind Tunnel Facility and Experimental Model

All experiments for this study were performed in the Florida State Flow Control (FSFC) wind tunnel. The FSFC is a modified Aerolab open-return wind tunnel with test section area of $30.5 \text{ cm} \times 30.5 \text{ cm}$ and a length of 61.0 cm . A variable frequency drive fan provides the flow through the tunnel, in which the freestream speed is monitored by a Pitot-static probe and a PID controller adjusts the drive frequency to maintain the desired wind speed. The flow is conditioned by an aluminum honeycomb mesh and two fine, anti-turbulence screens upstream of the 9:1 smooth contraction.

To prevent leading edge separation over the flat plate model, the cross-section of the leading edge of the plate is a 4:1 ellipse. However, the trailing edge of the model is square, which results in bluff-body shedding downstream. The flat plate model spans the entire width of the test section, the chord dimension is $c=40.2 \text{ cm}$, and the height is $h=0.095c$. The freestream velocity is set to $U_\infty=3.9 \text{ m/s}$ such that the Reynolds number with respect to chord dimension is $Re_c=10^5$. The freestream turbulence intensity integrated from 4 Hz to 1.25 kHz at this flow speed is $u'/U_\infty=0.5\%$. A schematic of the plate with relevant dimensions is shown in Figure 1.

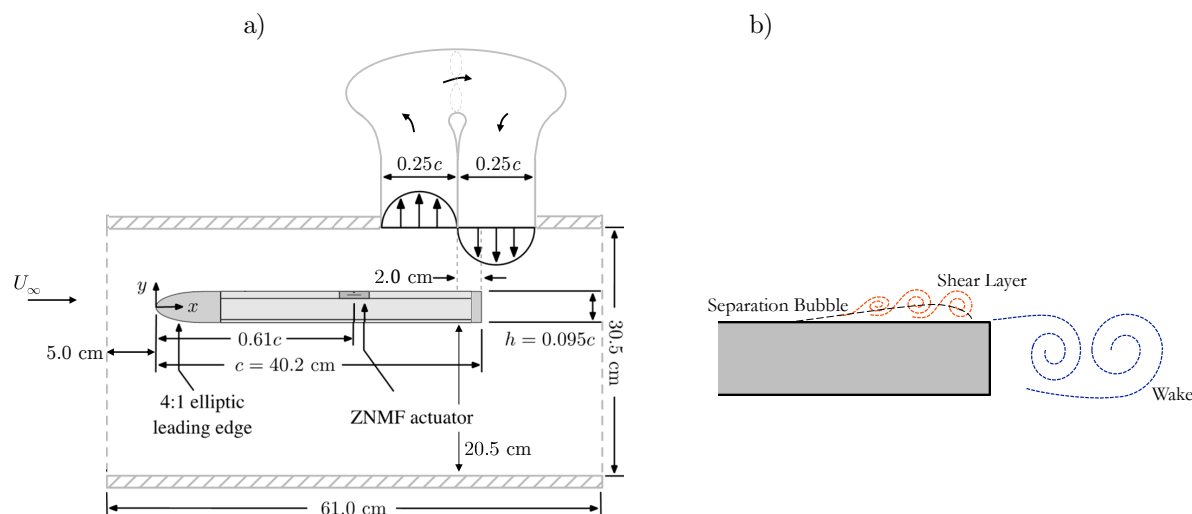


Figure 1. a) Schematic of the flat plate model and flow separation system. b) Representation of the shear layer, separation bubble, and wake, which are active regions of the flow with coupled dynamics. .

To produce separation, an adverse pressure gradient is generated by a zero-net suction/blowing boundary condition imposed on the ceiling of the wind tunnel test section. The boundary condition is imposed by a variable speed fan mounted within a closed-return duct system on the ceiling of the test section. The streamwise location of the flow separation can be altered by repositioning the model within the wind tunnel test section and changing the separation duct fan speed. For this study, the flow separation is induced in the aft portion of the model, such that a closed separation bubble is generated in a time-averaged sense, and the reattachment location is near the trailing edge (the exact location of the mean separation and reattachment points are provided in section B).

B. Actuation

The separated flow is subject to external forcing by a rectangular slot zero-net mass-flux (ZNMF) actuator embedded in the upper surface of the model at $x/c=0.61$. The ZNMF jet sequentially ingests and expels the surrounding air from a thin rectangular slot by the expansion and contraction of a cavity underneath the slot. This results in a non-zero time-averaged momentum flux, with zero time-averaged mass flux.¹⁸ Varying the cavity volume is achieved by driving four piezoelectric disks (APC Inc., PZT5J, Part Number: P412013T-JB) mounted spanwise on the floor of the cavity. The slot area of the actuator is $2 \text{ mm} \times 177.8 \text{ mm}$.

1. Actuator Characterization

The actuator is driven by a periodic burst modulation waveform that is defined by a burst frequency, carrier frequency, duty cycle, and amplitude. The carrier signal is a single sine wave that oscillates at the carrier frequency f_c , and is cycled on and off impulsively at the burst frequency f_b . The duty cycle is the ratio of the time the carrier signal is on over the total period of the burst. The nominal duty cycle of the modulation is set to 50%. However, in order to prevent spectral leakage and unanticipated high-frequency content, the duty cycle can vary from this slightly to ensure that an integer number of carrier cycles exists within the burst period.

Prior to conducting experiments, the output of the actuator is determined when driven by a single sine wave of various forcing frequencies and amplitudes. For each case, the RMS velocity of the actuator is determined by constant temperature hot-wire anemometry, in which the hot-wire probe is placed at the exit plane, on the centerline of the actuator slot. Two distinct resonant peaks in the rms velocity occur at approximately 700 and 2100 Hz. Therefore, for high output while reducing the risk of actuator damage, the carrier frequency is chosen to be near the second resonant peak of the actuator at $f_c = 2050$ Hz.

The output of the actuator subject to the burst modulated waveform is expressed in terms of the momentum coefficient (c_μ), which is defined as

$$c_\mu = \frac{A_j v_{rms}^2}{A_{sep} U_\infty^2}. \quad (1)$$

In this definition, A_j is the area of the actuator slot, and A_{sep} is the baseline (uncontrolled) separation region planform area (the length of the mean separation region, L_{sep} multiplied by the span of the plate). The RMS velocity of the jet is calculated from hot-wire measurements taken for various burst modulation waveforms. The forcing frequency is nondimensionalized with respect to the separation bubble length and freestream velocity as

$$F^+ = \frac{f_b L_{sep}}{U_\infty}. \quad (2)$$

C. Unsteady Pressure Sensors

Noting the extremely low value of freestream dynamic pressure, $O(10 \text{ Pa})$, unsteady surface pressure fluctuations are measured using an array of flush-mounted Panasonic WM-61A electret microphones. The pressure sensors have a nominal diameter of 6 mm; however the diameter of the exposed microphone diaphragm is 2 mm. The microphone locations are mounted within the separation region, from $x/c=0.7$ to $x/c=0.94$ in steps of 0.02 along the mid-plane.

Microphone excitation is provided by a National Instruments PXI 1042Q chassis and an NI PXI-4498 data acquisition card is used to digitize the pressure signal. This card provides built-in anti-aliasing. The microphone sample rate for this work is 8192 kHz and the duration of the measurements are 30 s. The response of the WM-61A microphone saturates over 130 dB ($p_{ref} = 20 \mu\text{Pa}$). However the maximum overall sound pressure level (OASPL) measured for this laminar separated flow is below 86 dB. Therefore, the measured fluctuations are well within the linear range of the WM-61A microphones.

1. Sensor Contamination Attenuation

Since the purpose of the surface mounted pressure sensor array is to extract relevant information regarding the separated flow dynamics from measurements of hydrodynamic pressure fluctuations, any extraneous signals that do not stem from the flow physics need to be removed. Examples of such content include the acoustic contamination from the wind tunnel drive fan and the separation duct fan, wind tunnel freestream unsteadiness, and electronic line noise.

In the experiment, identification of the contamination signals are achieved by installing microphones near the source of the disturbances. The contamination signals can be removed in post-processing to decontaminate the surface pressure measurement. For this case, reference microphones are installed near the wind tunnel drive fan, in the separation duct near, and on the floor of the wind tunnel upstream of the model. Unfortunately, measurements of the contaminant sources may be mutually correlated with the other sources, which must be accounted for. Therefore, conditional spectral analysis is employed to extract the uncorrelated component of each contaminant signal.^{19, 20}

If the j^{th} pure contamination signal is denoted by U_j , and the measurements of the contaminants are denoted by subscripted X , the decontamination process is described using the notation from¹⁹ as

$$U_j = X_{j,r!} = X_{j,(r-1)!} - L_{rj} X_{r,(r-1)!}. \quad (3)$$

The subscript convention $X_{j,r!}$ for the conditioned spectra can be interpreted as “ X_j conditioned by all of the previous X_r ”. The transfer function L_{rj} is estimated using the computed cross-spectra between the j^{th} and r^{th} contaminant measurements. Once all three of the contaminant signals are conditioned, their Fourier transforms are subtracted from the surface microphone measurements to determine the Fourier transform of the pure, uncontaminated signal.

D. Time-Resolved PIV

Time-Resolved Particle Image Velocimetry (TR-PIV) measurements of the separated flow are acquired by synchronized high speed laser and camera equipment. The measurement plane is oriented in the x - y plane, grazing the top surface of the flat plate, with a streamwise extent of $x/c \approx 0.66$ to $x/c \approx 1.01$, and height of $y/c \approx 0.1$. Olive oil particle seeding is introduced to the flow by a TSI 9307-6 atomizer. The nominal size of the olive oil particles is $1 \mu\text{m}$.²⁶ The particles are illuminated by a New Wave Pegasus SN 60022 Nd-YLF laser operating in a double-pulse configuration and images of the illuminated particles are acquired by a Phantom v411 high speed camera. For the current sample rate, the resolution of the images is 1280×800 pixels. The PIV images are acquired in both a frame-straddled configuration and a time-series configuration. For the frame-straddled approach, images are acquired at 3200 fps. The time between the laser pulses for a sin-

gle TR-PIV acquisition is $\Delta t = 180 \mu s$. This results in one PIV vector field per every two image acquisitions, so the effective PIV sample rate is 1600 Hz. For the time-series configuration, images are acquired at 2500 fps. In this case, the velocity vector fields are computed in between each image, so the effective PIV sample rate for the time-series mode is 2500 Hz.

Once images are acquired, image preprocessing and vector calculations are performed using LaVision DaVis 8.1.x.²⁵ For image preprocessing, a sliding background subtraction filter is employed to reduce background image contamination. Then, a particle intensity normalization is applied to reduce non-uniform illumination. A direct cross-correlation is performed across interrogation windows of the image pairs to determine the particle shift. This process is iterated for successively smaller interrogation windows. The final interrogation window size is 16×16 pixels with 75 % overlap, which results in a vector resolution of 0.466 mm per vector.

The correlation-statistics method for estimating PIV uncertainty³⁵ is employed due to its utility and implementation in the velocity vector calculation in the LaVision DaVis software. This method provides an estimate of the random uncertainty of PIV velocity vectors at every grid point for each snapshot by exploiting the fact that the converged correlation function between a PIV image pair should be symmetric about its maximum. Thus, the uncertainty is estimated via the observed asymmetry in the computed correlation function,³⁵ which is defined as the difference between corresponding sidelobe levels of the correlation function. Relating this to measurement error is accomplished by computing the residual velocities that result from the asymmetries within the interrogation window, and then the standard deviation of the residual velocities is computed for each interrogation window. The uncertainty of the mean flow and turbulent quantities are determined by propagating the snapshot uncertainties provided by the correlation-statistics method. The maximum uncertainty in the mean flow field is 0.14 % of the freestream velocity and the maximum uncertainty of the variance of the velocity is 0.34% of the maximum variance within the flow field (with 95% confidence).

III. Dynamic Mode Decomposition

Several variants of the Dynamic Mode Decomposition (DMD) are utilized in this work. As an analysis tool, DMD is used to identify the spatially coherent modes that correspond to the characteristic frequencies of the baseline uncontrolled separated flow. DMD is also used to characterize the flow response to actuation by applying DMD with control (DMDc).²⁸

DMD derives a linear system from measurements that approximate the transition matrix from an arbitrary snapshot to the next snapshot in time.^{16,31} This can be described as an estimate of the Koopman operator of the measured dynamics.^{30,36} The spatial modes are the eigenvectors of this derived system, and the temporal characteristics of the modes are derived from the eigenvalues. Recently, Taira et al.³⁴ has compiled a comprehensive overview of modal decomposition techniques applied to fluid flows. The authors provide a practical overview of DMD and its connections to other energy (POD) and dynamic (Koopman analysis, resolvent analysis, etc) based decomposition approaches.

Since exact state snapshots are not available in experimental settings, measurements must be taken that sufficiently capture possible system states. These measurements are denoted by italics as \mathbf{x}_k . The linear transition matrix provided by performing DMD on the set of measurements is labeled \mathbf{A}_{DMD} , in which

$$\mathbf{x}_{k+1} = \mathbf{A}_{DMD} \mathbf{x}_k. \quad (4)$$

For the current study, DMD will be employed on flow data acquired by both PIV and surface pressure measurements, in which m simultaneous measurements are made, and a total of n snapshots are recorded. Organizing the data for DMD begins with arranging the measurements into current and previous snapshot matrices. The previous snapshot matrix is denoted as \mathbf{X} , and each simultaneous observation is arranged as a column of the snapshot matrix in which the subscript refers to the temporal step, resulting in an $m \times n - 1$ matrix. The current snapshot matrix is defined similarly as \mathbf{Y} . The snapshot matrices are provided below

$$\mathbf{X} = \begin{bmatrix} | & | & & | \\ \mathbf{x}_1 & \mathbf{x}_2 & \cdots & \mathbf{x}_{n-1} \\ | & | & & | \end{bmatrix}, \quad \mathbf{Y} = \begin{bmatrix} | & | & & | \\ \mathbf{x}_2 & \mathbf{x}_3 & \cdots & \mathbf{x}_n \\ | & | & & | \end{bmatrix}. \quad (5)$$

Based on these definitions,¹⁶ the DMD modes and eigenvalues are equal to eigenvectors and eigenvalues of

$$\mathbf{A}_{DMD} := \mathbf{Y} \mathbf{X}^+, \quad (6)$$

where the superscript $+$ denotes the pseudoinverse.

For no modal truncation, the number of DMD modes and eigenvalues will be $\min(m, n)$. For the case in which it is expected that fewer states are required to capture the dynamics, a reduced problem can be formulated by taking the singular value decomposition (SVD) of the snapshot matrix $\mathbf{X} = \mathbf{U} \mathbf{\Sigma} \mathbf{V}^*$ and substituting into 6,

$$\mathbf{A}_{DMD} = \mathbf{Y} [\mathbf{U} \mathbf{\Sigma} \mathbf{V}^*]^+ = \mathbf{Y} \mathbf{V} \mathbf{\Sigma}^+ \mathbf{U}^*. \quad (7)$$

The dimensional reduction is performed by truncating the SVD of \mathbf{X} to include only the first r singular values, in which a subscript r will denote a truncated matrix. From this, the reduced proxy system matrix can be determined by

$$\tilde{\mathbf{A}} = \mathbf{U}_r^* \mathbf{A}_{DMD} \mathbf{U}_r = \mathbf{U}_r^* \mathbf{Y} \mathbf{V}_r \boldsymbol{\Sigma}_r^+ \quad (8)$$

Performing the dimension reduction presents one with the question of how to properly determine the value for r . This is the subject of ongoing research. However, for the present case, power spectrum derived from surface pressure measurements and previous studies indicate that at least 3 oscillatory phenomena exist simultaneously in the baseline flow.⁷ Since the DMD modes derived are complex conjugate pairs, at least 6 modes are required to capture 3 oscillatory phenomena. In order to surpass this criterion while keeping the computational burden low, $r=25$ for all of the PIV data utilized in the current study based on empirical observations. Since the number of simultaneous surface pressure measurements are much lower than the PIV measurements, no rank truncation is performed for DMD applied to surface pressure data.

A. Total Least Squares DMD

Since approximations of the Koopman operator are generated from measurements of nonlinear systems, a natural application of DMD is the dynamical analysis of flow measurements. However, applying the conventional DMD algorithm to noisy or “inexact” data yields a biased analysis—owing to an asymmetric treatment of erroneous data by standard DMD.¹⁴ Without knowledge of the levels of measurement noise, the total least-squares variant of DMD can be employed to mitigate these biases. Details regarding this variant of DMD are provided in the reference.

This procedure begins with constructing an augmented snapshot matrix as a combination of the current and previous snapshots:

$$\mathbf{Z} := \begin{bmatrix} \mathbf{X} \\ \mathbf{Y} \end{bmatrix}. \quad (9)$$

The snapshot matrices are then projected onto an r -dimensional space that is defined as the first r right singular vectors from the SVD of \mathbf{Z} . The projected snapshot matrices are denoted $\tilde{\mathbf{X}}$ and $\tilde{\mathbf{Y}}$ and the conventional DMD algorithm is then performed on these projected snapshot matrices.

The right eigenvectors of $\tilde{\mathbf{A}}_{DMD}$ are denoted as \mathbf{w}_i and the DMD modes are computed as $\phi_i = \bar{\mathbf{U}} \mathbf{w}_i$ (with corresponding eigenvalues λ_i).³⁰ The frequency and growth rate for the i^{th} mode is $f_i = f_s \angle \lambda_i / (2\pi)$ and $g_i = f_s \log |\lambda_i|$. The k^{th} value of the i^{th} Koopman eigenfunctions are approximated by the inner product of the left eigenvectors (\mathbf{w}_i) of \mathbf{A}_{DMD} and the k^{th} measurement:³⁰

$$\varphi_{i,k} = \mathbf{w}_i \mathbf{x}_k. \quad (10)$$

The DMD modes and DMD eigenfunctions are combined to reconstruct the observations:³⁰

$$\mathbf{x}_k = \sum_{i=1}^r \varphi_{i,k} \phi_i. \quad (11)$$

For this study, (unless otherwise noted) all observations of the separated flow are taken after transients have decayed. Thus, the oscillatory amplitude of the DMD modes are of primary interest with regard to the temporal analysis of the modal decomposition of the flow data. To quantify the relative oscillatory contribution of each mode, a modal amplitude is defined as follows. From equation 11, the contribution of mode i to the k^{th} observation is

$$\mathbf{x}_{i,k} = \varphi_{i,k} \phi_i. \quad (12)$$

The temporal standard deviation of $\mathbf{x}_{i,k}$ provides a measure of the fluctuating amplitude of the contribution of the i^{th} DMD mode and is defined by

$$\boldsymbol{\sigma}_i = \sqrt{\frac{1}{n} \sum_{k=1}^n (\mathbf{x}_{i,k} - \boldsymbol{\mu}_i)^2}. \quad (13)$$

In this expression, $\boldsymbol{\mu}_i$ is the mean of the quantity $\mathbf{x}_{i,k}$, which is computed by

$$\boldsymbol{\mu}_i = \frac{1}{n} \sum_{k=1}^n \mathbf{x}_{i,k}. \quad (14)$$

At this point, $\boldsymbol{\sigma}_i$ is a vector of the standard deviations of the contribution of the i^{th} DMD mode to each point in the original snapshot observation. The mean of this vector is taken to be the modal oscillatory amplitude of the DMD mode

$$\sigma_{DMD,i} = \bar{\boldsymbol{\sigma}}_i. \quad (15)$$

This allows for a comprehensive analysis of the baseline separated flow measurements. However, the addition of actuation serves to complicate the identified dynamical characteristics furnished by DMD. For these cases, DMD with control (DMDc) is implemented to separate the natural dynamics and the effect of forcing.²⁸

B. DMD with Control

For systems with no external inputs, current state observations are only a function of the previous state. However, this is not the case when forcing is introduced, and the natural state evolution should be separated from the influence of actuation. In this case, the linear discrete-time system provided by DMD takes the form

$$\mathbf{x}_{k+1} = \mathbf{A}_{DMD}\mathbf{x}_k + \mathbf{B}\mathbf{u}_k, \quad (16)$$

when provided state measurements \mathbf{x}_k and prescribed input signals \mathbf{u}_k . This can be expressed by appending the measurement matrix with the input array, resulting in

$$\mathbf{x}_{k+1} = \mathbf{A}_{DMD}\mathbf{x}_k + \mathbf{B}\mathbf{u}_k = \begin{bmatrix} \mathbf{A}_{DMD} & \mathbf{B} \end{bmatrix} \begin{bmatrix} \mathbf{x}_k \\ \mathbf{u}_k \end{bmatrix}. \quad (17)$$

This is rewritten in terms of the snapshot matrices as

$$\mathbf{Y} = \mathbf{G}_{DMD} \mathbf{\Omega}. \quad (18)$$

The terms introduced in this expression are defined as $\mathbf{G}_{DMD} := \begin{bmatrix} \mathbf{A}_{DMD} & \mathbf{B} \end{bmatrix}$ and $\mathbf{\Omega} := \begin{bmatrix} \mathbf{X} & \mathbf{U} \end{bmatrix}'$, in which \mathbf{U} is a matrix of the discrete input signals. This reverts the problem back to the form of conventional DMD; thus the appended DMD matrix (\mathbf{G}_{DMD}) is determined using an appropriate DMD algorithm (TDMD in this case). This process is referred to as DMD with control (DMDc).²⁸ An additional concern is raised if the governing dynamics of the separated flow are nonlinear. In this case, the identified DMD eigenvalues and modes will likely vary as external forcing is introduced. Monitoring the evolution of the forced dynamics in real time would allow for determining efficient control trajectories for reattaching the separated flow. However, the procedures outlined above are designed for a posteriori dynamical analysis and are not suited for providing on-line updates. This limitation is addressed with the development of online DMD.¹⁷ If high-fidelity observations of the flow are available at a rate sufficiently higher than the Nyquist frequency, online DMD can provide real-time updated estimates of the DMD eigenvalues and modes with each new measurement.

C. Online DMD

The formulations provided above for dynamic mode estimates from TDMD require the entire snapshot ensemble to be stored in memory. This can be prohibitive since thousands of snapshots may be required for accurate estimates. Therefore, ‘‘batch’’ processing DMD is limited by size of the snapshot matrix. The work by Hemati et al.²³ provides an alternative approach, in which the DMD eigenvalues and modes are computed and updated each snapshot by implementing a Gram-Schmidt process. The resulting DMD modes and eigenvalues are provided with much less computational effort and without requiring the rest of the snapshots be stored in RAM. A similar updating DMD implementation is developed in the work by Zhang et al.¹⁷ that has been named ‘‘Online DMD.’’ Instead of the Gram-Schmidt approach, online DMD takes advantage of the Sherman-Morrison formula.³² As with streaming DMD, online DMD provides modal updates with each new snapshot. However, one notable difference between streaming and online DMD is the ability for online DMD to discard the contribution of old snapshots in a precise and controllable manner. Thus, online DMD provides modes and eigenvalues that correspond to a limited number of snapshots, while streaming DMD retains the contributions of all past snapshots. This procedure allows for temporal variations in the dynamics to be accounted for with respect to the duration of the retained snapshots. In the context of the present work, the possibly nonlinear response of the separated flow to forcing will result in time-varying DMD modes and eigenvalues. Using online DMD provides ‘‘real time’’ updates to the dynamic characteristics as forcing is applied, which can be implemented in adaptive and robust control strategies.

The formulation of online DMD begins with the definition of the DMD transition matrix (6), and the property of the pseudoinverse. $\mathbf{X}^+ = \mathbf{X}^T[\mathbf{X}\mathbf{X}^T]^{-1}$,

$$\mathbf{A} = \mathbf{Y}\mathbf{X}^+ = \mathbf{Y}\mathbf{X}^T[\mathbf{X}\mathbf{X}^T]^{-1} = \mathbf{Q}\mathbf{P}. \quad (19)$$

The new matrices are defined as, $\mathbf{Q} := \mathbf{Y}\mathbf{X}^T$ and $\mathbf{P} := [\mathbf{X}\mathbf{X}^T]^{-1}$. If a new snapshot $(\mathbf{x}_{k+1}, \mathbf{y}_{k+1})$ is to be included in the snapshot matrix, \mathbf{Q} and \mathbf{P} can be appended as

$$\begin{aligned} \mathbf{Q}_{k+1} &= [\mathbf{Y} \ \mathbf{y}_{k+1}][\mathbf{X} \ \mathbf{x}_{k+1}]^T = \mathbf{Q} + \mathbf{y}_{k+1}\mathbf{x}_{k+1}^T, \quad \text{and} \\ \mathbf{P}_{k+1} &= ([\mathbf{X} \ \mathbf{x}_{k+1}][\mathbf{X} \ \mathbf{x}_{k+1}]^T)^{-1} = [\mathbf{P}^{-1} + \mathbf{x}_{k+1}\mathbf{x}_{k+1}^T]^{-1}. \end{aligned}$$

The expression for \mathbf{P}_{k+1} is in a form that can be computed by the Sherman-Morrison formula,

$$\mathbf{P}_{k+1} = [\mathbf{P}^{-1} + \mathbf{x}_{k+1}\mathbf{x}_{k+1}^T]^{-1} = \mathbf{P} - \gamma \mathbf{P}\mathbf{x}_{k+1}\mathbf{x}_{k+1}^T\mathbf{P}. \quad (20)$$

The scalar, γ is defined as $\gamma := 1/(1 + \mathbf{x}_{k+1}^T \mathbf{P} \mathbf{x}_{k+1})$. Therefore, given current estimates of \mathbf{Q} and \mathbf{P} , the DMD transition matrix can be updated for new snapshots by $\mathbf{A}_{k+1} = \mathbf{Q}_{k+1} \mathbf{P}_{k+1}$, after some substitution (see ¹⁷),

$$\mathbf{A}_{k+1} = \mathbf{A} + \gamma (\mathbf{y}_{k+1} - \mathbf{A} \mathbf{x}_{k+1}) \mathbf{x}_{k+1}^T \mathbf{P}. \quad (21)$$

For the initial case in which there is no current estimate for \mathbf{A} and \mathbf{P} , \mathbf{A}_0 can be initialized randomly, and $\mathbf{P}_0 = \alpha \mathbf{I}$ in which the parameter α is very large so $\mathbf{P}_0^{-1} \approx \mathbf{0}$.

As mentioned earlier, there may be scenarios in which it is desired that old snapshots be discarded from the current DMD calculation. Such a case may arise if the DMD eigenvalues exhibit a drastic departure from the initial state due to a nonlinear response to forcing. If all of the contributions from the old snapshots are retained in this situation, the resulting DMD eigenvalues and modes would be an average of the baseline and forced system. To address this, a weighting factor is introduced to allow for the contribution of old snapshots to be gradually discarded, resulting in refreshed dynamical estimates from online DMD. Consider the weighted snapshot matrices,

$$\boldsymbol{\chi} = \begin{bmatrix} | & | & & | \\ (\sqrt{\lambda})^{n-1} \mathbf{x}_1 & (\sqrt{\lambda})^{n-2} \mathbf{x}_2 & \dots & \mathbf{x}_{n-1} \\ | & | & & | \end{bmatrix}, \quad \boldsymbol{\psi} = \begin{bmatrix} | & | & & | \\ (\sqrt{\lambda})^{n-1} \mathbf{x}_2 & (\sqrt{\lambda})^{n-2} \mathbf{x}_3 & \dots & \mathbf{x}_n \\ | & | & & | \end{bmatrix}.$$

The weighting factor (λ) is set so older snapshots are either aggressively ($\lambda \rightarrow 0$) or gradually ($\lambda \rightarrow 1$) diminished. By defining a DMD transition matrix relative to the weighted snapshot matrices $\mathbf{A}_W = \boldsymbol{\psi} \boldsymbol{\chi}^+$, the online DMD formulation can be carried out as before ¹⁷. The end result is that the weighting factor penalizes the updated value of \mathbf{P}_{k+1} as so,

$$\mathbf{P}_{k+1} = \frac{1}{\lambda} (\mathbf{P} - \gamma \mathbf{P} \mathbf{x}_{k+1} \mathbf{x}_{k+1}^T \mathbf{P}). \quad (22)$$

This approach is useful for real time DMD estimates as long as the computational effort required to update the DMD estimates remains low. Online DMD requires $\mathcal{O}(m^2)$ operations in updating the DMD estimates.¹⁷ Thus, this algorithm is well suited to the low-dimensional surface pressure measurements, in contrast to streaming DMD which is beneficial for high-dimensional data. More information regarding the relative time required for various DMD algorithms is provided in Zhang et al.¹⁷ It should be noted that this approach is formulated for cases in which there is no external forcing. However online DMD can also be implemented for control cases by appending the DMD matrix as outlined in the previous section.

The measurement and data analysis methods outlined in this and the previous sections are applied in order to characterize the baseline separated flow. In doing so, pressure and velocity data are acquired for the unforced separated flow, and the mean, spectral, and DMD characteristics are presented in the following chapter.

IV. Analysis of the Baseline Separated Flow

The natural, unforced separated flow is analyzed to provide a baseline with which flow control experimental results will be compared. As noted in the introduction, the spatio-temporal evolution of the baseline flow is described in terms of the combination and interaction of three distinct flow phenomena.⁵ These phenomena are illustrated in Figure 1-b and consist of the shear layer vortex roll-up, the separation bubble, and wake shedding. For this study, PIV and unsteady surface pressure data provide a means for visualizing the interaction of these phenomena. This section provides baseline results beginning with surface pressure measurements to identify the spectral content of the flow. Then, attention is turned to full-field flow evaluation from PIV measurements. Finally, DMD is applied to PIV and pressure measurements in order to identify the quantities that are critical for observing the states required for control.

The mean velocity profile upstream of the separation point is extracted from the PIV snapshots, and the shape factor is estimated as $H = 2.67$ at $x/c \approx 0.3$. Comparing this to $H = 2.59$ for the Blasius boundary layer indicates that the flow is laminar upstream of separation.

PIV is implemented near the ceiling of the wind tunnel test section to measure the velocity at the inlet and outlet of the separation duct. The magnitude of the suction and blowing velocity, along with the location of the plate relative to the inlet and outlet of the separation duct define the size and location of the separation region. For the current study, the plate is positioned in the test section 6 cm from the ceiling and the trailing edge is approximately 2 cm from the midline of the separation system. This position relative to the separation system results in an average separation bubble length of $L_{sep} = 0.23c$.

A. Unsteady Pressure

The unsteady pressure fluctuations within the separated flow are recorded by microphones that lie near the mean recirculation region. Baseline experiments were performed in which the surface pressure sensor array is simultaneously sampled at $f_s = 8192$ Hz for 30 seconds for the baseline separated flow. The frequency content of the unsteady pressure

is analyzed by computing the power spectral density of the measured signal by Welch's method.¹⁹ The block size for the PSD computation is 8192 samples, which results in a frequency binwidth of $\Delta f = 1$ Hz. PSD will be plotted with respect to Strouhal number

$$St_{L_{sep}} = fL_{sep}/U_{\infty}. \quad (23)$$

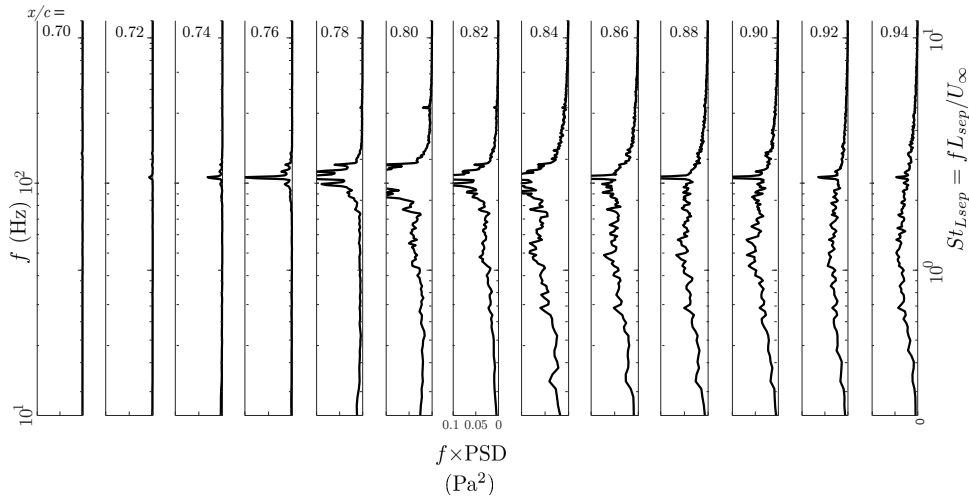


Figure 2. Premultiplied power spectral density plots of the corrected surface mounted microphone array measurements after the contaminating signals have been removed. The microphone location for each plot is denoted at the top of the plot.

Recall from section 1 that the surface pressure microphones may be contaminated by extraneous pressure fluctuations. In this case, the likely candidates for contamination are acoustic noise from the wind tunnel drive fan, acoustic noise from the separation duct fan, and freestream unsteadiness. The tunnel drive fan microphone is mounted near the fan housing, removed from any flow inside the wind tunnel. The separation duct fan microphone is mounted inside the separation duct, downstream of the suction fan. Finally, a microphone is mounted in the floor of the wind tunnel, just downstream of the initial contraction. Since this microphone is exposed to the wind tunnel flow but removed from the flat plate model and boundary layer, any fluctuations in the freestream will be registered by this microphone. This provides a reference for removing freestream unsteadiness from the surface mounted microphone array. This microphone is referred to as the tunnel floor microphone.

The contaminants are removed from the array microphone signals by the process described in section 1. The corrected, premultiplied power spectral density plots for the microphone array are provided with fixed axis limits to show the streamwise development of the oscillatory content in Figure 2. This shows the spatial evolution of the Kelvin-Helmholtz instability into a distinct preferred frequency of $St_{L_{sep}} = 2.51$ which reaches a maximum amplitude at $x/c = 0.8$. The peak begins to decay near the mean reattachment region as the flow transitions to turbulent flow, and spectral broadening occurs.

B. PIV

PIV snapshots provide spatially resolved mean and turbulent quantities of the baseline flow. Since a high speed PIV system is utilized, the sample rate of the velocity snapshots is much higher than the characteristic frequencies of the flow. Thus, frequency spectrum estimates can be extracted from the flow field data by Fourier analysis or DMD. The TR-PIV dataset for the uncontrolled, canonical separated flow ($Re_c = 10^5$) studied here consists of at least $m = 6000$ snapshots, each with $n = 19778$ number of vectors per snapshot. The minimum PIV sample rate for this study is 1600 Hz. Figure 3 contains vorticity contours of the mean of the PIV snapshots. The separation region is illustrated by the line of $\bar{u} = 0$, depicted as the black dashed line. The length of the mean separation bubble is found to be $L_{sep} = 0.23c$.

Turbulent statistics are computed from the PIV snapshots and provided in Figure 4 as contours of the standard deviation and covariance of the u and v velocity components. These plots show that fluctuation levels increase dramatically in the shear layer, downstream of the separation point. This along with the apparent thickening of the mean shear layer (Figure 3) indicate enhanced turbulent mixing in this region.

TDMD is applied to the TR-PIV snapshots of the baseline separated flow in order to identify global dynamical characteristics of the flow. TDMD extracts flow phenomena from measurements of the flow in the form of DMD spatial modes. The resulting characteristic frequencies and modal amplitudes are quantified.

TDMD is performed using a rank-reduction level $r = 25$, which corresponds to retaining over 99% of the fluctuating kinetic energy content based on an SVD of \mathbf{X} . Figure 5 contains the DMD eigenvalues plotted on the positive

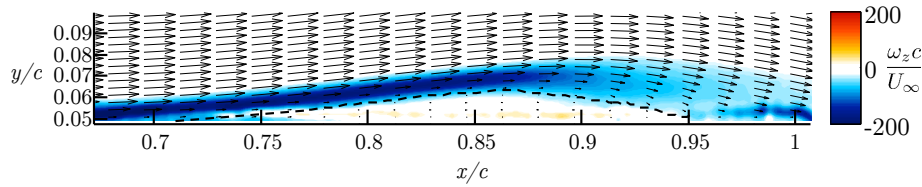


Figure 3. Average z -vorticity as computed from PIV snapshots. The line of $\bar{u}=0$ is the black dashed line.

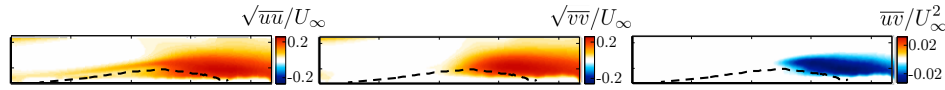


Figure 4. Turbulence statistics. The line of $\bar{u}=0$ is superimposed to illustrate the separation region.

quadrant of the complex plane alongside the modal oscillatory amplitude plotted with respect to Strouhal number and dimensional frequency (Hz). This plot shows that the dominant modes extracted via TDMD are non-decaying and purely oscillatory (i.e., the eigenvalues lie very close to the unit circle). This is expected due to the oscillatory, stable limit cycle characteristics of the separated flow.

Additionally, the highest modal amplitude occurs at $St_{L_{sep}} = 2.53$. The PSD estimates of the velocity probe and unsteady pressure data provided in the previous section corroborates the existence of this frequency content. This DMD mode describes the most energetic component of the limit cycle of the baseline separated flow. In Figure 6, the real part of the DMD modes are visualized as vorticity contours. The spatial mode for $St_{L_{sep}} = 2.53$ is composed of patterned, coherent vorticity structures. Since the DMD modes are complex, computing the phase and magnitude of the dominant DMD mode lends additional insight. The result of this is presented in Figure 7. The spanwise variation of the phase within the active region of the mode indicates traveling wave characteristics. This is due to the convection of vortices generated by the separated shear layer.

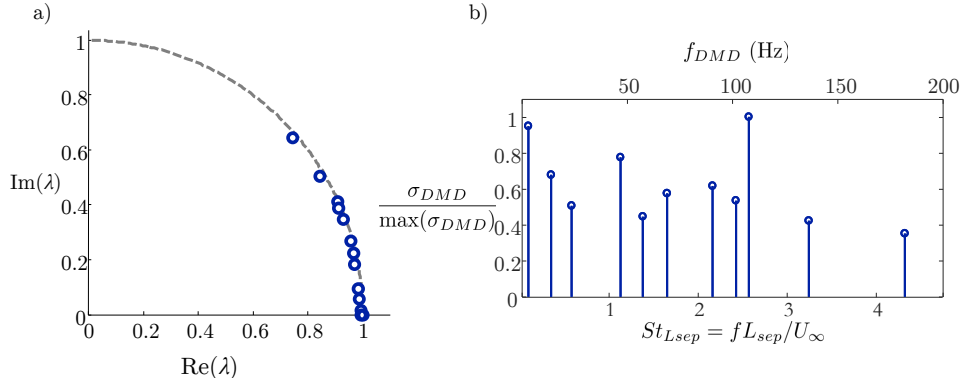


Figure 5. a) DMD eigenvalues plotted on the first quadrant of the complex plain. b) RMS values of the DMD eigenfunctions plotted with respect to $St_{L_{sep}}$.

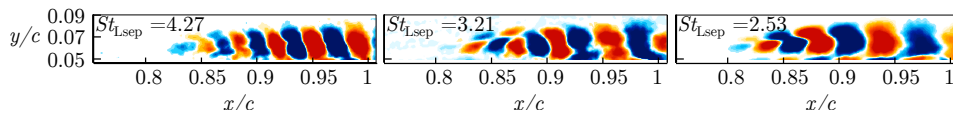


Figure 6. Real part of the vorticity of the DMD modes corresponding to the three highest frequencies identified by TDMD.

While the dynamic characteristics provided by performing DMD on velocity field measurements by PIV are valuable for visualizing the natural evolution of the flow measurements, these results are too cumbersome to be included in a real time feedback control scheme. However, unsteady surface pressure measurements can be acquired and processed much more efficiently and may be a candidate for real-time state estimation of the separated flow. Therefore, pressure informa-

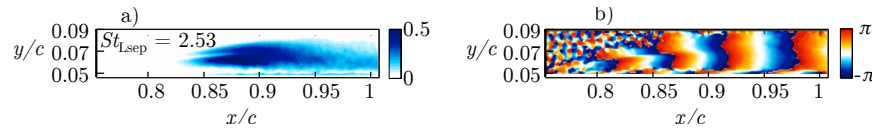


Figure 7. a) Magnitude and b) phase of the vorticity of the dominant DMD mode. The frequency of this mode is $St_{Lsep} = 2.53$.

tion will now be vetted to determine if the modal characteristics of the separated flow can be extracted with sufficient clarity. To this end, an estimate of the full pressure field is computed from the velocity field PIV measurements. Then, DMD is applied to the pressure field snapshots in order to compare the dynamical results provided by flow velocity information.

C. Pressure Field via Poisson's Equation

In order to determine the degree to which the dynamical characteristics of the separated flow are attainable from pressure measurements, the evolution of the pressure field is estimated by solving the Pressure-Poisson equation. The dynamically relevant modes of the pressure field are determined using DMD applied to the pressure snapshots. The pressure field DMD results will then be used to guide the manner in which the surface mounted pressure sensor array will be utilized for state estimation.

The work by de Kat and van Oudheusden²⁴ demonstrates that time-resolved, planar PIV can be used to estimate the pressure field snapshots of 2-Dimensional flows. The Pressure-Poisson equation is derived by taking the divergence of the Navier-Stokes equations for momentum conservation in incompressible flows.

The unsteady term is identically zero due to the incompressible flow assumption, while viscous terms are neglected due to their relatively small and inherently noisy contribution due to spatial derivatives.²⁷ Also, since PIV measurements for the current study provide 2-component planar velocity fields, the Laplacian of the pressure fluctuations is computed assuming two-dimensional flow

$$\nabla^2 p_{xy} = \frac{\partial^2 p}{\partial x^2} + \frac{\partial^2 p}{\partial y^2} = -\rho \left[\left(\frac{\partial u}{\partial x} \right)^2 + 2 \frac{\partial u}{\partial y} \frac{\partial v}{\partial x} + \left(\frac{\partial v}{\partial y} \right)^2 \right]. \quad (24)$$

However, for turbulent flows that exhibit 3-D fluctuations, the two-dimensional flow assumption introduces an error, as noted by de Kat and van Oudheusden.²⁴ This insight suggests that the pressure field determined by Equation (24) from the current planar PIV data will be less reliable within the turbulent region. In solving for p_{xy} , an Eulerian approach is adopted in which discrete estimates of the x and y partial derivatives necessary for the right hand side of Equation (24) are estimated using a second-order central difference scheme from a single PIV snapshot.

At the boundaries, one-sided differences are computed with Neumann boundary conditions defined for the edges of the domain. For grid points adjacent to the plate surface, zero pressure gradient is enforced in the vertical direction. All boundary conditions are defined to satisfy the inviscid momentum equation. The pressure computational grid is a subset of the PIV measurement domain that consists of 259×34 uniformly arranged points. The conjugate gradient method³³ is used to solve Equation (24) for the instantaneous p_{xy} .

The results of this analysis are shown in Figure 8, in which mean-subtracted pressure contours are superimposed with synchronized vorticity fields. These plots show that low pressure regions convect along with the vortices from the shear layer. Time is nondimensionalized using the characteristic frequency of the Kelvin-Helmholtz vortex rollup identified by the PSD of the surface pressure sensors (106 Hz).

The DMD eigenvalues for the pressure field snapshot data are compared to those of the velocity field PIV snapshots in Figure 9, in which the dominant modal frequency identified from both sets match. The dynamic modes identified by TDMD for the pressure field snapshots are provided in figure 10. Note the similarities in the dominant pressure field mode to that of the velocity field from figure 7. As with the PIV modes, the phase variation in the pressure modes indicates traveling wave characteristics. Additionally, the lack of variation in the transverse direction suggests that the critical information regarding the separation characteristics can be gleaned from only considering streamwise profiles of the DMD modes. Thus, the separated flow modalities should be available from measurements provided by the streamwise array of surface mounted pressure sensors. The next section provides the results of analyzing these measurements.

D. Unsteady Surface Pressure DMD

The results of section C show that performing DMD on pressure field snapshots yields similar dynamical characteristics to that of PIV. This suggests that DMD applied to both measurements provide approximation of the same Koopman operator.³⁷ Also, section A shows that the dominant DMD mode frequency emerges as a peak in the power spectrum of the surface microphone array. Due to this correspondence and the fact that these separated flow pressure modes likely leave a footprint on the surface of the model, a profile representation of the DMD modes can be obtained from the measurements of the surface pressure array microphones. To test this hypothesis, DMD is performed on

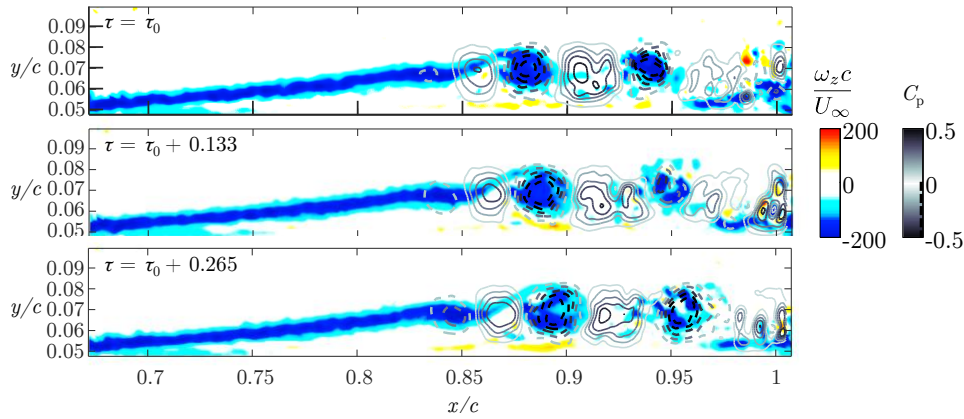


Figure 8. Snapshots of vorticity superimposed with mean-subtracted pressure contours computed from the 2-D PIV vector field. Negative pressure contours are depicted by dashed lines. Regions of low pressure convect with the vortices that are generated by the separated shear layer.

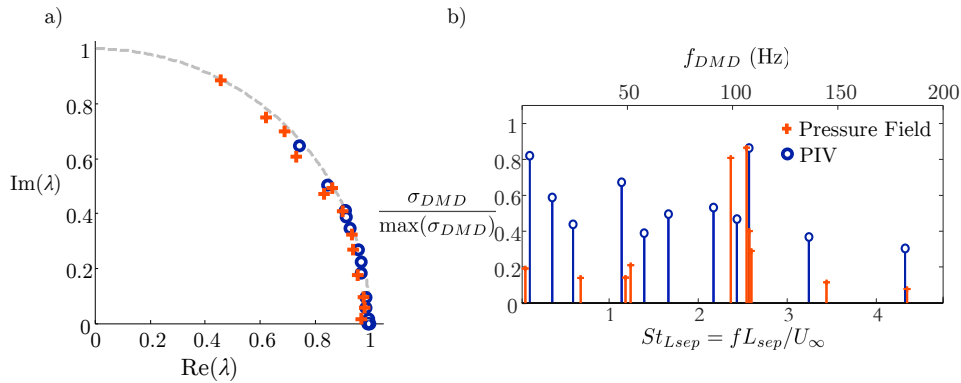


Figure 9. a) DMD eigenvalues and b) modal amplitude identified by TDMD of the pressure field snapshots superimposed with the results of applying DMD to the PIV snapshots.

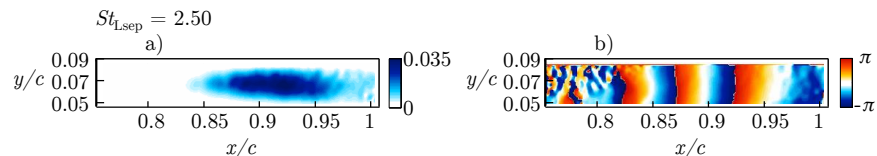


Figure 10. a) Magnitude and b) phase of the dominant DMD mode identified by TDMD of the pressure field.

the simultaneously sampled pressure data. Before DMD is applied, the signals are corrected for noise contamination (see section 1 and section A), and the data are digitally low pass filtered to 500 Hz and downsampled to 2048 Hz to remove high frequency acoustic content from the actuator.

Typically, for the case of dynamical analysis of PIV measurements, as many snapshots as possible are retained when performing DMD. This ensures that the eigenvalues and modes identified by DMD are statistically converged. However, the eventual goal for the pressure array data is to have DMD applied in real time to provide updates to the dynamical characteristics as actuation is applied. Thus, DMD results need to be obtained for a limited number of snapshots. To identify the number of samples required for reliable dynamical estimates, a qualitative convergence study is performed. DMD modes and eigenvalues are estimated by online DMD for increasing numbers of surface pressure array snapshots. Then, the frequency is computed from these estimates. The weighting factor (λ , see section C) is set to unity for these initial computations to ensure that there is no snapshot attenuation in the DMD computations. Then, from these results the weighting factor can be chosen such that the appropriate number of

samples are retained to provide reliable real-time updates of the dynamics.

Since the surface pressure microphone array is comprised of 13 sensors, 13 eigenvalues are obtained from the online DMD computation. This allows for a maximum of 7 distinct frequencies to be identified. Figure 11 shows the frequencies computed from the identified DMD eigenvalues from online DMD with a weighting factor of unity (no attenuation).

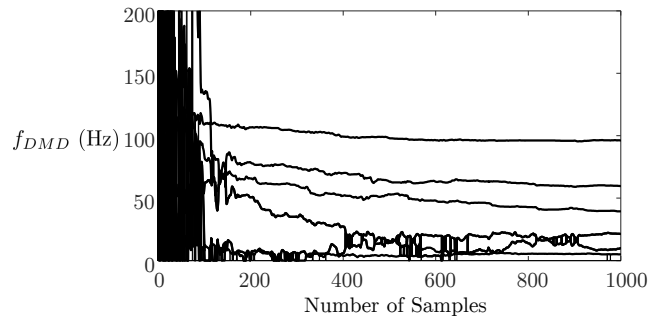


Figure 11. Frequencies computed from the identified DMD eigenvalues for increasing number of snapshots from online DMD, $\lambda=1$.

The frequency estimates determined from online DMD begin to settle after about 100 samples, then appear sufficiently converged after 350 samples. Three primary frequencies exist, along with some low frequency content that exhibit apparent mode switching. The eigenvalues plotted on the complex plane and modal amplitude plotted with respect to identified frequency is shown in Figure 12 for 350 samples. As with DMD of the PIV data, the dominant frequency at $St_{Lsep}=2.47$ corresponds to the periodic shear layer vortex generation.

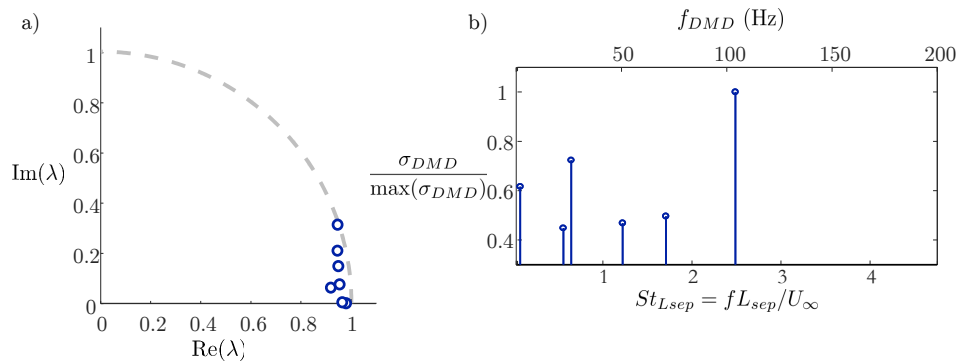


Figure 12. DMD eigenvalues plotted on the first quadrant of the complex plain (a) and DMD modal amplitude plotted with respect to frequency (b) estimated by online DMD of 350 surface pressure measurements with $\lambda=1$.

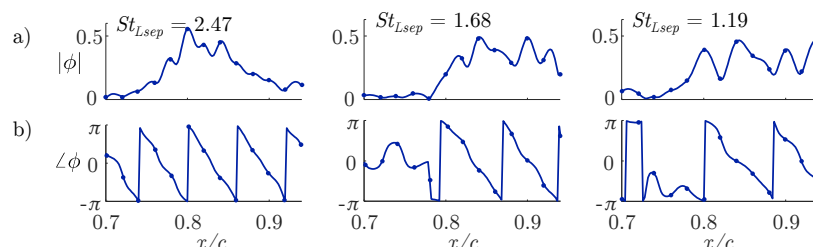


Figure 13. a) Magnitude and b) phase of the first three DMD modes identified by online DMD from 350 snapshots of surface pressure data and $\lambda=1$. The corresponding DMD frequencies are provided with each plot.

The magnitude and phase of the DMD modes computed from online DMD are provided in Figure 13. The dominant mode profile exhibits spatial periodicity, indicative of traveling wave characteristics. These results compare favorably to the structure of the DMD modes computed from PIV measurements in Figure 6, and the corresponding pressure

field DMD modes in Figure 10. Specifically, the dominant DMD mode identified by both the PIV measurements and surface pressure measurements corresponds to the convection of the large vortices pinched off of the separated shear layer.

Several studies have shown that effective separation control strategies exploit the most amplified frequency of the shear-layer instability.^{9–13,22} Since the dynamical characteristics of the separated flow (including the modality of the vortex generation due to the Kelvin-Helmholtz instability) are identified by the surface pressure measurements, the pressure array DMD results may be viable for state estimation in closed loop control of the separated flow. To illustrate how this can be implemented to provide dynamical characteristics on the fly, online DMD is performed for the surface microphone measurements of the baseline separated flow with the weighting factor λ set to 0.996. This provides attenuation of at least 50% after 350 samples ($\tau \approx 18$), and an attenuation level of 99% after about 1500 samples ($\tau \approx 80$). This allows for the DMD matrix to be updated with each new sample, while tracking temporal variations in the measured dynamics. In other words, a time varying, linear model of the nonlinear separated flow is provided in real time from surface pressure measurements. The results of performing online DMD for the baseline separated flow are presented in Figure 14. The DMD frequencies are updated for each new measurement, and are plotted for a duration of 100 time units. Time is nondimensionalized with respect to the characteristic frequency of the Kelvin-Helmholtz vortex rollup identified by the PSD of the surface pressure sensors (106 Hz).

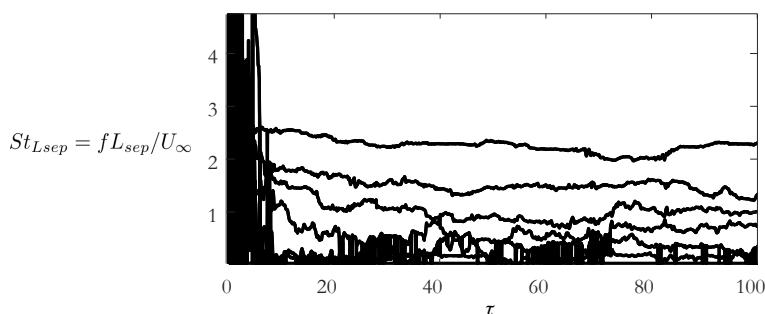


Figure 14. DMD frequencies identified by online DMD with a weighting factor of $\lambda=0.996$.

After the erroneous content due to the algorithm initialization has decayed, the identified DMD frequencies exhibit some wandering, possibly due to wind tunnel unsteadiness. By setting the weighting factor to $\lambda=0.996$, the primary frequency varies between 82 and 107 Hz over the duration shown. This indicates that a stationary optimal forcing frequency may not exist. Thus, control should be applied using information from real time estimates of the flow states to track any natural variations in the dynamics.

However, the variation of the identified frequencies provided by online DMD would be reduced if the weighting factor is increased, and should be tuned based on the desired time response of the DMD updates. Setting the weighting factor too low results in increased sensitivity to measurement errors and disturbances. However, setting the factor too high results in slowly updated dynamics. In implementing online DMD for real-time updates of the dynamics as the separated flow is forced, the weighting factor should be set just low enough to meet the performance criteria of the controller. This way, the maximum number of samples are retained in the DMD estimation.

In the following section, PIV measurements and fluctuating surface pressure measurements are used to address the response of the flow to actuation. Then, Online DMD is applied to the surface pressure measurements to provide the temporal evolution of the model estimates of the flow to account for nonlinear changes in the dynamics due to actuation.

V. Open Loop Separation Control

Targeting the natural dynamics of separated flow has been shown to be an effective strategy for reducing separation^{13,22}. Experiments are conducted in which forcing is applied while simultaneously measuring the surface pressure fluctuations from the microphone array described in section C. To assess the impact actuation has on the entire flow field, PIV data are acquired synchronously with the microphone array. Two momentum coefficients are tested, $C_\mu = 6.6 \times 10^{-5}$ and $C_\mu = 2.8 \times 10^{-4}$. As a performance metric, the height of the mean reversed flow region is determined from PIV measurements for each forcing frequency (i.e., an indication for the size of the separation bubble) and plotted in Figure 15.

With the aim of reducing the separation region, forcing at $F^+ = 2.43$ exhibits the best performance for both actuation amplitudes. However, a sharp increase in separation height is shown for forcing slightly above the optimal frequency ($F^+ = 2.56$). These frequencies are both sufficiently close to the frequency identified to be the dominant shear layer frequency. In fact, Figure 14 provides evidence that the natural variation of the dominant frequency encompasses both

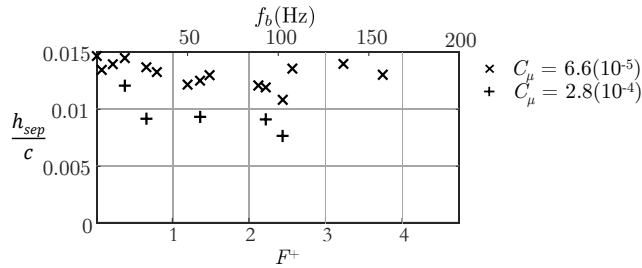


Figure 15. Normalized mean separation height plotted against input frequency. $F^+ = 0$ corresponds to the uncontrolled baseline separation height. The minimum mean separation height measured corresponds to forcing at the dominant frequency identified by TDMD from both pressure and PIV measurements, $F^+ = 2.43$.

of these forcing frequencies. Therefore, PIV data will be analyzed to draw additional details regarding performance of these forcing conditions. In all, four cases will be examined more carefully: $F^+ = 2.43$ and $C_\mu = 2.8 \times 10^{-4}$, $F^+ = 2.43$ and $C_\mu = 6.6 \times 10^{-5}$, $F^+ = 0.36$ and $C_\mu = 6.6 \times 10^{-5}$, and $F^+ = 2.56$ and $C_\mu = 6.6 \times 10^{-5}$. Of these cases, the $F^+ = 2.43$ cases correspond to the optimal control cases for both momentum coefficients and the $F^+ = 0.36$ and $F^+ = 2.56$ cases will be referred to as suboptimal. A plot containing the mean vorticity fields for these cases is provided in Figure 16-a.

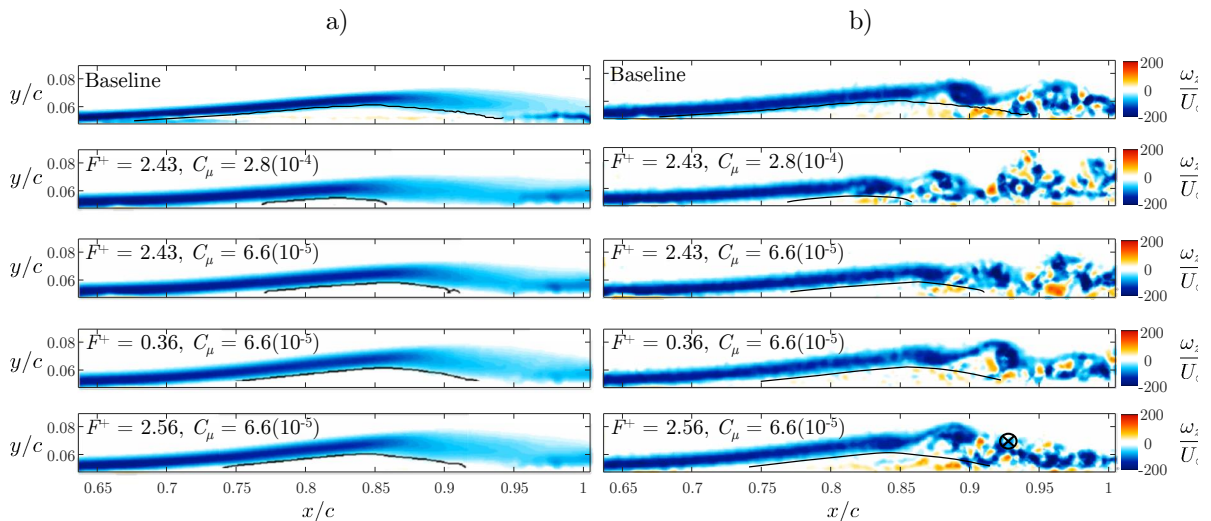


Figure 16. Contour plots of normalized a) mean and b) instantaneous z -vorticity, for select forcing cases and snapshots. The line of $\bar{u}/U_\infty = 0$ is superimposed on the contours to illustrate the extent of the separation region. The $F^+ = 2.43$ cases exhibit the most reduced separation height of all of the forcing frequencies in this study. Regarding the instantaneous plots, the $F^+ = 2.43$, high momentum coefficient case exhibits earlier vortex destabilization than the other cases. The separated shear layer is higher for the $F^+ = 0.36$ and $F^+ = 2.56$ cases.

Select instantaneous vorticity snapshots are provided in Figure 16-b. These plots provide some insight regarding the shear layer dynamics subject to forcing for the optimal and suboptimal cases. The baseline separation exhibits coherent vortices from the shear layer that convect downstream. Eventually, the vortex breaks into turbulent structures, which results in mean flow reattachment. The instantaneous vorticity snapshots for the $F^+ = 2.43$ cases show earlier turbulent transition, allowing the flow to re-energize and reattach further upstream. This process is enhanced for the higher momentum coefficient case. However, for the suboptimal cases ($F^+ = 0.36$ and $F^+ = 2.56$), the turbulent transition does not appear to occur much earlier than for the baseline. Also, the instantaneous shear layer trajectories appear notably higher than for the optimal forcing cases.

Finally, the PIV measurements of the evolution of the separated flow subject to forcing are phase-averaged with respect to the actuation signal. This allows for visualization of the coherent response of the flow to actuation. The phase is defined with respect to the actuator burst signal, in which zero phase occurs when the signal switches from zero to one. The mean-subtracted vorticity is shown for a phase angle of zero in Figure 17-a. Additionally, the mean-subtracted, phase-averaged z -vorticity at $x/c \approx 0.93$, $y/c \approx 0.07$ (depicted by the black marker in Figure 16-b) is plotted with respect to

the phase of the actuation burst frequency f_b in Figure 17-b. The phase-averaged burst modulator signal (A_b) is plotted beneath each vorticity plot. For $A_b=1$, the actuation is applied, and a value of $A_b=0$ indicates that the actuator is off.

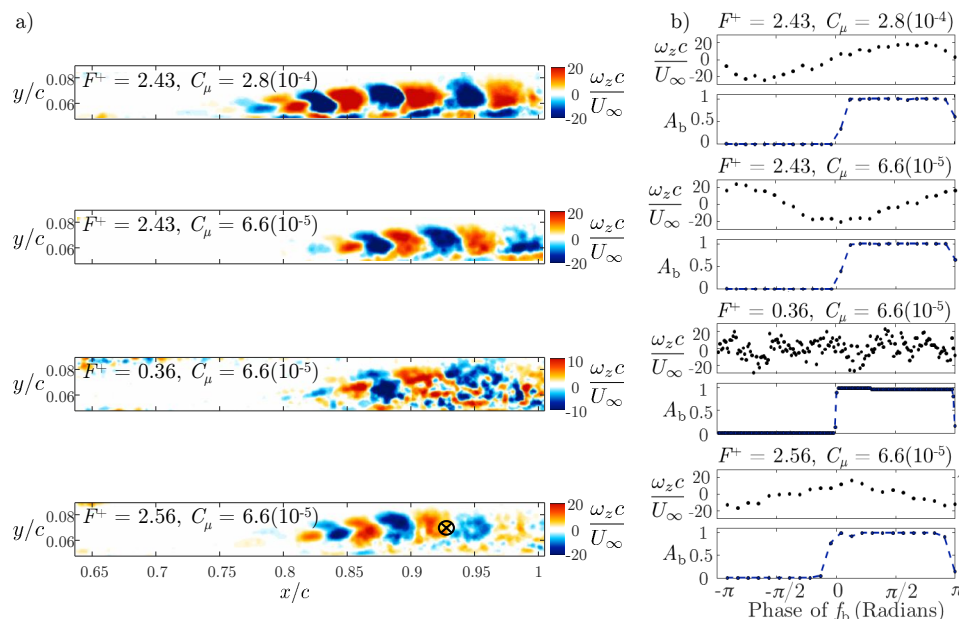


Figure 17. a) Vorticity fields of mean-subtracted phase-averaged PIV velocity fields for select forcing cases for a phase angle of 0 and b) mean-subtracted, phase-averaged z -vorticity at $x/c \approx 0.93$, $y/c \approx 0.07$ (position denoted by black marker) plotted with respect to the phase of the actuation burst frequency f_b . The phases are defined with respect to the forcing burst frequency, and the phase-averaged burst modulator signal (A_b) is plotted beneath each vorticity plot (blue dashed line). The control cases are labeled for each plot. The $F^+ = 2.43$ cases exhibit coherent vortical structures, in which the higher forcing results in stronger vorticity levels, and earlier development. The low frequency ($F^+ = 0.36$) case contains some evidence of structure, although weaker than the optimal cases, and the $F^+ = 2.56$ case contains structures that appear to lose strength further upstream than the optimal control cases ($F^+ = 2.43$). The high frequency cases all show correlated signals between the phase-averaged vorticity and actuation signal, with different relative lags. The low frequency ($F^+ = 0.36$) case appears to take on some periodicity within the actuation period, though the frequency may be doubled. The increased error due to reduced number of samples for this case prevents any definitive conclusions.

The phase-averaged vorticity contours for both of the $F^+ = 2.43$ cases show coherent structures that are reminiscent of the shear layer DMD mode. For this frequency, the flow responds favorably to increased forcing amplitude, as the vortical structures are stronger, develop earlier, and persist longer for the higher forcing level. Thus, forcing at this frequency serves to amplify the natural shear layer vortex generation of the separated flow. Interestingly, even though the flow becomes turbulent earlier for these cases, the coherence with the actuator persists through the turbulent region, indicating that the actuator is still affecting the flow past the transition point. Regarding the phase-trace of the vorticity at $x/c \approx 0.93$, $y/c \approx 0.07$, all three of the high frequency cases show correlated signals between the phase-averaged vorticity and actuation signal, with different relative lags.

Coherent structures are still present for the low frequency case ($F^+ = 0.36$). However the wavelength is notably longer, and the strength of the structures is reduced as small-scale features and turbulent fluctuations are disbursed throughout the separated flow region. The observed behavior is partially attributed to the lower number of samples available per phase with respect to the data for the higher frequency forcing. Specifically, for the lowest frequency case ($F^+ = 0.36$), there are 37 samples per phase, whereas the phase averages for the highest forcing frequency ($F^+ = 2.56$) are estimated by 249 snapshots per phase. Therefore, the lower frequency phase average estimates will contain higher uncertainty than the high frequency cases. This is evident in Figure 17 by the increased spatial variance in the $F^+ = 0.36$ case. The increased uncertainty due to the reduced number of samples for this case prevents any definitive conclusions, and further analysis is required.

Finally, the case in which the frequency is slightly higher than optimal shows some early development of Kelvin-Helmholtz-like structures. However, the coherence breaks down more quickly. This behavior suggests that the support for the actuation enhanced shear layer vortex formation quickly degrades when forcing at suboptimal frequencies - specifically when the frequency is higher than the natural vortex formation frequency. This sensitivity to forcing frequency supports the desire for real-time updates to the dynamical estimates as forcing is applied. The data acquired from the surface mounted microphone array are used to enable quick, data-driven time-varying linear estimates of the

evolution of the separated flow using online DMD. The temporal variations of the modal characteristics are provided in the next section.

VI. Online System Identification of Separated Flow Subject to Forcing

Tracking the variations in the dynamical characteristics as forcing is applied to the separated flow is accomplished by performing online DMD to the surface microphone array data. Since it was shown in section D that at least 350 samples are needed for accurate modal estimates from online DMD, the weighting factor (λ) for the following computations is set to 0.996. This allows for the dynamics to be updated with each new sample, while tracking the effect of forcing. Also, for every $\tau=80$ time units, the DMD estimates are essentially fully refreshed.

Therefore, any nonlinear variations in the system that occur as the flow is forced will be accounted for as the DMD estimates are updated. This provides a linear, time-varying system estimation of the nonlinear separated flow given observations of the fluctuating surface pressure. To test the ability of online DMD to provide updated system estimates of the forced flow, the unsteady surface pressure was measured by the surface mounted microphone array for the cases explored earlier. As mentioned previously, the update step of online DMD requires $\mathcal{O}(m^2)$ operations, which took an average of 0.19 milliseconds in the current implementation using MATLAB on a desktop PC with dual 6 core processors. This allows for updates at a rate of around 5 kHz. The temporal evolution of the frequencies identified by online DMD is presented for these cases in Figure 18.

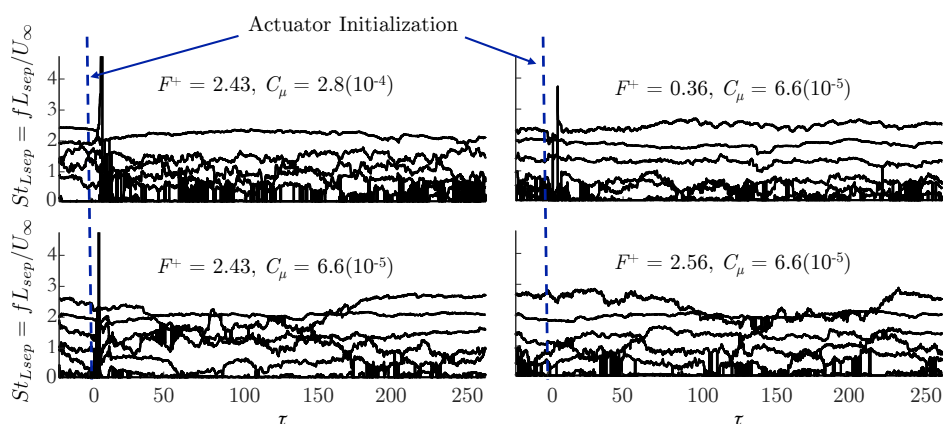


Figure 18. Temporal evolution of the DMD frequencies identified by online DMD from surface pressure measurements of separated flow subject to forcing. The forcing parameters are provided at the top of each plot. Zero time indicates when actuation begins, and is depicted by the blue dashed line.

The plots of Figure 18 show that shortly following the beginning of the actuation, a sharp perturbation occurs in the identified frequencies. This can be attributed to the fact that transients are developing within the flow due to actuator initiation. Once transients have decayed, the frequencies identified for the high momentum, $F^+ = 2.43$ Hz case are relatively steady for the time period shown, particularly for the highest frequency mode. However, both of the low momentum, high forcing frequency cases exhibit a slow variation in DMD frequency. This variation may be indicative of the flow not fully locking on with the forcing frequency, which may be improved with higher momentum coefficient. Also, the degree to which the variations are observed will depend on the value of the weighting factor.

This shows that online DMD can update the dynamical estimates of the nonlinear variations in the separated flow as forcing is applied. Since this is done quickly, using simple microphone measurements, efforts are underway to develop adaptive, closed-loop control methods for autonomously delaying and reducing separated flow.

VII. Conclusions

In an effort to develop a framework for sensing and controlling separated flow that is potentially resilient to variations in flow conditions, a method was tested that identifies dominant system dynamics in real time from a linear array of 13 surface pressure measurements beneath a laminar separation bubble. It was found that the DMD modes and eigenvalues provided by pressure are consistent with the full-field DMD results from PIV measurements. Thus, the convective phenomena characterizing the separated flow are sufficiently captured by the linear, surface mounted microphone array embedded within the separation region. A new procedure called online DMD was employed that efficiently provides updates to the DMD system matrix as new measurements are available. This algorithm was used to provide a linear representation of the evolution of the pressure measurements, after the surface pressure measurements were conditioned to remove contamination.

Applying online DMD to the baseline flow measurements revealed a slow variation in the estimated DMD frequencies, possibly due to wind tunnel unsteadiness. This is significant since separation control studies often attempt to identify

a stationary characteristic frequency at which to apply forcing. This suggests that the best attempt at determining an effective open loop forcing frequency based on the natural oscillations of the flow is a statistical estimate of the characteristic frequencies. One way to mitigate this is by providing real-time estimates of the flow states to the control algorithm. Furthermore, for the forcing levels provided here, the open loop control performance exhibits significant sensitivity to the forcing frequency. This provides further incentive for closed-loop approaches to mitigating flow separation.

Regarding the control cases provided here, actuation is provided by a ZNMF jet. Analysis of PIV measurements of the separated flow subject to forcing indicate that separation reduction is accompanied with accelerated turbulent transition. Optimal forcing tends to enhance the natural shear layer vortex generation and subsequent breakdown to turbulence. For the current study, online DMD reveals that the one of the momentum coefficients tested may be too low for stationary control in some cases. This is evident by the slow variation in DMD frequencies seen for the low C_μ cases, which may indicate intermittent lock-on to the forcing frequency.

Online DMD on the pressure measurements of the forced flow allows for the nonlinear system response to forcing to be characterized as a time-varying linear system. Since this is possible with simple microphone measurements, at frequencies much higher than the characteristic frequencies of the flow, this approach can be used for state feedback, and model estimation for closed-loop control methods for mitigating separated flow.

VIII. Acknowledgments

Funding for this work is provided under AFOSR Grant FA9550-14-1-0289, monitored by Dr. Doug Smith.

References

- ¹ Seifert, A., Bachar, T., Koss, D., Shepshelovich, M., Wygnanski, I. "Oscillatory Blowing: A Tool to Delay Boundary-Layer Separation." *AIAA Journal* 31 (11), 2052-2060, 1993
- ² Seifert, A., Darabi, A., Wygnanski, I. 1996 "Delay of airfoil stall by periodic excitation". *Journal of Aircraft* 33 (4), 691-698, 1996.
- ³ Seifert, A., Pack, L. G., "Oscillatory Control of Separation at High Reynolds Numbers." *AIAA Journal* 37 (9), 1062-1071, 1999.
- ⁴ Glezer, A., Amitay, M., Honohan, A. "Aspects of low- and high-frequency aerodynamic flow control." *AIAA Journal* 43 (7), 1501-1511, 2005
- ⁵ Mittal, R., Kotapati, R. "Resonant mode interaction in a canonical separated flow." In *IUTAM Symposium on Laminar-Turbulent Transition* (ed. R. Govindarajan), pp. 341-348. Springer, 2006.
- ⁶ Raju, R., Mittal, R. Cattafesta, L. "Dynamics of Airfoil Separation Control Using Zero-Net Mass-Flux Forcing". *AIAA Journal* 46 (12), 3103-3115. 2008
- ⁷ Mittal, R., Kotapati, R. B., Cattafesta III, L. N. "Numerical study of resonant interactions and flow control in a canonical separated flow." In *43rd AIAA Aerospace Sciences Meeting and Exhibit*. AIAA, Reno, Nevada, 2005
- ⁸ Kotapati, R., Mittal, R., Cattafesta, L., "Numerical study of a transitional synthetic jet in quiescent external flow", *Journal of Fluid mechanics* 581 (1), 287-321. 2007
- ⁹ Yarusevych, S., Kawall, J. G., Sullivan, P. E., "Airfoil Performance at Low Reynolds Numbers in the Presence of Periodic Disturbances", *Journal of Fluids Engineering* Vol. 128, May 2006.
- ¹⁰ Postl, D., Balzer, W., Fasel, H. F. "Control of laminar separation using pulsed vortex generator jets: direct numerical simulations." *Journal of Fluid Mechanics* 676, 81-109, 2011.
- ¹¹ Yarusevych, S., Kotsonis, M., "Steady and Transient Response of a Laminar Separation Bubble to Controlled Disturbances", *J. Fluid Mech*, vol. 813, 2017.
- ¹² Marxen, O., Kotapati, R., Mittal, R., Zaki, T., "Stability analysis of separated flows subject to control by zero-net-mass-flux jet", *Physics of Fluids* 27, 2015.
- ¹³ Griffin, J., Oyarzun, M., Cattafesta, L. N., Tu, J. H., Rowley, C. W., Mittal, R., "Control of a Canonical Separated Flow" *AIAA* 2968, 2013
- ¹⁴ Hemati, M. S., Rowley, C. W., Deem, E. A., and Cattafesta, L. N., "De-Biasing the Dynamic Mode Decomposition for Applied Koopman Spectral Analysis of Noisy Datasets," pre-print, arXiv:1502.03854, 2015
- ¹⁵ Tu, J. H., Rowley, C. W., Aram, E. Mittal, R., "Koopman spectral analysis of separated flow over a finite-thickness flat plate with elliptical leading edge", In *49th AIAA Aerospace Sciences Meeting*. AIAA, Orlando, Florida, 2011.
- ¹⁶ Tu, J. H., Rowley, C. W., Luchtenburg, D. M., Brunton, S. L., Kutz, J. N., "On Dynamic Mode Decomposition: Theory and Applications", *Journal of Computational Dynamics*, 1-2, 391-421, 2014
- ¹⁷ Zhang, H., Rowley, C., Deem, E., Cattafesta, L., "Online dynamic mode decomposition for time-varying systems", preprint, 2017.
- ¹⁸ Holman, R., Utturkar, Y., Mittal, R., Smith, B. L., and Cattafesta, L., "Formation criterion for synthetic jets," *AIAA journal*, Vol. 43, No. 10, pp. 2110-2116, 2005
- ¹⁹ Bendat, J. S., Piersol, A. G., "Random Data Analysis and Measurement Procedures", Wiley, Hoboken, NJ, 2010
- ²⁰ Bendat, J. S., Piersol, A. G., "Engineering Applications of Correlation and Spectral Analysis, 2nd Edition", Wiley, Hoboken, NJ, 2010
- ²¹ Griffin, J., "On the control of a canonical separated flow" Ph. D. Thesis, University of Florida, 2013
- ²² Hemati, M. S., Deem, E. A., Williams, M. O., Rowley, C. W., and Cattafesta, L. N., "Improving Separation Control with Noise-Robust Variants of Dynamic Mode Decomposition," *54th AIAA Aerospace Sciences Meeting*, California, 2016.

- ²³ Hemati, M., Williams, M., Rowley, C., “Dynamic mode decomposition for large and streaming datasets”, *Physics of Fluids* 26, 2014.
- ²⁴ de Kat, R., van Oudheusden, B. A., “Instantaneous planar pressure determination from PIV in turbulent flow”, *Exp Fluids* 52:1089-1106, 2012.
- ²⁵ LaVision, “DaVis v8.1.x” 2013.
- ²⁶ Melling, A., “Tracer Particles and Seeding for Particle Image Velocimetry,” *Meas. Sci. Technol.*, Vol. 8, pp. 1406-1416, 1997.
- ²⁷ van Oudheusden, B. A., Scarano, F., Roosenboom, E. W. M., Casimiri, E. W. F., Souverein, L. J., “Evaluation of integral forces and pressure fields from planar velocimetry data for incompressible and compressible flows”, *Exp Fluids* 43:153-162, 2007.
- ²⁸ Proctor, J., Brunton, S., Kutz, J., “Dynamic Mode Decomposition with Control” *SIAM J. Applied Dynamical Systems*, V. 15, N. 1, pp 142-161, 2016.
- ²⁹ Rathay, N. W., Boucher, M. J., Amitay, M., Whalen, E., “Performance Enhancement of a Vertical Tail Using Synthetic Jet Actuators” *AIAA Journal* Vol. 52, No. 4, April 2014
- ³⁰ Rowley, C. W., Mezić, I., Bagheri, S., Schlatter, P., Henningson, D., “Spectral analysis of nonlinear flows”, *J. Fluid Mech.*, Vol. 641 pp. 115-127, 2009.
- ³¹ Schmid, P., “Dynamic mode decomposition of numerical and experimental data”. *J. Fluid Mech.* vol. 656, 2010.
- ³² Sherman, J., Morrison, W., “Adjustment of an inverse matrix corresponding to a change in one element of a given matrix”, *The Annals of Mathematical Statistics*, vol. 21, no. 1, pp. 124-127, 1950
- ³³ Shewchuk, J., “An Introduction to the Conjugate Gradient Method Without the Agonizing Pain” August 4, 1994.
- ³⁴ Taira, K., Brunton, S., Dawson, S., Rowley, C., Colonius, T., McKeon, B., Schmidt, O., Gordeyev, S., Theofilis, V., Ukeiley, L., “Modal Analysis of Fluid Flows: An Overview”, arXiv:1702.01453, 2017.
- ³⁵ Wieneke, B., “PIV Uncertainty Quantification from Correlation Statistics.” *Measurement Science and Technology* 26(074002), 2015.
- ³⁶ Williams, M. O., Kevrekidis, I. G., Rowley, C. W., “A Data-Driven Approximation of the Koopman Operator: Extending Dynamic Mode Decomposition” arXiv:1408.4408, 2014.
- ³⁷ Williams, M. O., Rowley, C. W., Mezić, I., Kevrekidis, I. G., “Data Fusion via Intrinsic Dynamic Variables: An Application of Data-Driven Koopman Spectral Analysis” arXiv:1411.5424, 2014.